

Verification and application of numerically generated magnetic coordinate systems in gyrokinetics

P. Xanthopoulos¹, D. Mikkelsen², F. Jenko³, W. Dorland⁴ and O. Kalentev¹

¹*Max-Planck-Institut für Plasmaphysik, Teilinstitut Greifswald,
EURATOM Association, Wendelsteinstr. 1,
D-17491 Greifswald, Germany*

²*Plasma Physics Laboratory, Princeton University,
Princeton, New Jersey 08543-0451, USA*

³*Max-Planck-Institut für Plasmaphysik, Teilinstitut Greifswald,
EURATOM Association, Boltzmannstr. 2,
D-85748 Garching, Germany*

⁴*University of Maryland, College Park, Maryland 20742, USA*

Abstract

In the context of linear gyrokinetic simulations, an analysis of the application of field-aligned coordinate systems generated numerically from magneto-hydrodynamic equilibria is presented. This family of systems allows some flexibility in the choice of the coordinates, and gyrokinetic solvers often differ in this respect. Certain transformations are therefore required in order to compare physics results. Accordingly, benchmarks of a linear microinstability are carried out between two similar gyrokinetic codes. Effort is also put on the verification of the special properties of the generated systems through certain diagnostics.

1 Introduction

Since the perpendicular transport in magnetized plasmas is very slow compared to the parallel one, microinstabilities and microturbulence are very extended along the magnetic field. Hence, both linear and nonlinear gyrokinetic simulations benefit greatly from the use of field-aligned (also known as magnetic) coordinate

systems [1]. This setup requires expanding several differential operators on these adapted coordinates and computing a set of geometric components.

In the past, linear and nonlinear gyrokinetic benchmarks were performed (see e.g. [2, 3, 4, 5]) considering a circular cross section axisymmetric configuration or Miller-type equilibria [6], which have been proposed to capture effects of plasma shaping and finite aspect ratio. In these cases, all geometric terms can be evaluated analytically, and code-code comparisons are straightforward as far as magnetic geometry is concerned. However, for many situations of practical interest – like non-axisymmetry or proximity to the plasma edge – the necessity to employ magnetohydrodynamic (MHD) equilibria arises. Here, there exists some flexibility in choosing appropriate coordinates, as well as different ways to determine the geometric information required for gyrokinetic simulations. This fact turns code benchmarks into a subtle enterprise.

Although the constant increase in computing power significantly alleviates the burden of turbulence simulations, linear gyrokinetics remain a quite active field of study (see e.g. [7, 8, 9, 10]). The present work involves two frequently used gyrokinetic codes – in their linear mode of operation – GENE [11] and GS2 [12], which solve the same set of equations but differ in the description and numerical implementation of the magnetic geometry. Our goal is to pinpoint and subsequently resolve incompatibilities which emerge naturally in the context of linear gyrokinetic calculations, once MHD equilibria are employed.

The remainder of this paper is organized as follows. In Section 2, on the basis of an axisymmetric MHD equilibrium, we describe two coordinate systems differing with respect to the definition of the surface label. The numerical generation of these systems is accomplished through a field line tracing (FLT) technique [13], implemented in the code TRACER [14]. The characteristics of these systems are verified through several diagnostics. Subsequently, each coordinate system is applied to the gyrokinetic code GENE, in order to determine the linear properties (growth rates and frequencies) of an Ion Temperature Gradient (ITG) instability. The interpretation of the results has twofold scope, acting as a consistency check for the TRACER/GENE platform itself, as well as indicating the method of benchmarking simulation results from codes which follow different approaches to address the geometry.

Indeed, such a case is presented in Section 3, where we perform an analogous study, this time involving both gyrokinetic codes GENE and GS2. The relations connecting the geometric elements between the two approaches are analytically derived and numerically evaluated. In view of the incompatibility between the geometric descriptions, care has to be exercised when the issue of benchmarking the corresponding simulation results arises. In this context, it will become clear that the proper assignment of the key parameters controlling the instability is of major importance. In Section 4, we recapitulate the main findings of this work.

2 Comparison of geometric quantities and gyrokinetic results between two magnetic coordinate systems

In this section, we numerically generate two magnetic coordinate systems, based on data from the DIII-D tokamak device (shot number 126848) [15]. This comprises an EFIT (g-style) file, which provides the equilibrium information, coupled with a database (iterdb.126848_woNBI), which contains the radial profiles of several experimentally determined quantities. The coordinate systems, described in detail below, are constructed using the code TRACER and subsequently applied to the gyrokinetic code GENE, in order to simulate a typical linear ITG instability. Consistency requires that we obtain identical results (in terms of growth rates and frequencies) for both cases, provided that the two systems are correctly mapped against each other. Therefore, this exercise introduces the benchmarks between the codes GENE and GS2, which utilize different coordinate systems.

2.1 Description and numerical generation of coordinate systems

In the following, the properties of the magnetic coordinate systems are described, in the framework of flux tube gyrokinetics. We also provide details concerning the numerical generation of the systems via the FLT method (for more information, the reader is referred to [14]).

2.1.1 Flux Coordinate System (FCS)

This is a standard flux coordinate system, namely the surface label is defined through a flux quantity. Specifically, we consider the coordinates (ρ, ν, χ) , where $\rho = \sqrt{\frac{\Psi_t}{\pi B_a}}$ (in units of meters). Here, Ψ_t denotes the toroidal flux and $B_a = 1.8955T$ is the value of the vacuum toroidal magnetic field at the geometric axis. By construction, the coordinate χ follows the field line and is related to the toroidal angle ϕ through the relation $d\chi = d\phi/q$, so $\chi \in [-\pi, \pi]$.

Our goal is to construct the Clebsch representation for the magnetic field line which generates the flux tube,

$$\mathbf{B} = B_a \nabla \rho \times \nabla \nu \quad (2.1)$$

where $\nu = \frac{\Psi_{p0}}{2\pi B_a}(q\theta - \phi)$. As usual, θ stands for the poloidal angle and q is the safety factor. Also, Ψ_{p0} is the poloidal flux evaluated at the surface $\rho = \rho_0$, where the field line belongs and in the neighborhood of which the flux tube is located (thereafter, the same convention applies to all quantities with the subscript “0”). Note that in the representation (2.1) both Clebsch coordinates ρ and ν carry dimensions of length.

The FLT procedure performs the transformation from the cylindrical system (r, ϕ, z) to the FCS (ρ, ν, χ) . This involves the numerical solution of a linear system of ordinary differential equations, in the form of an initial value problem. In practice, starting from an initial point with cylindrical coordinates $(r_{in}, \phi_{in}, z_{in})$ (in the axisymmetric case currently under study, the value of ϕ_{in} is arbitrary), the field line is equally followed in both forward ($\chi > 0$) and backward ($\chi < 0$) directions until one poloidal transit is completed. The coordinates r_{in} and z_{in} are determined by the requirement that the initial point lies on the surface $\rho = \rho_0$ and also in the midplane of the device, where $B_r = 0$ holds. Hence, we prescribe the quantities $\nabla\rho|_{in}$ and $\nabla\nu|_{in}$ at the initial point, in a form which guarantees the generation of a coordinate system suitable for describing a configuration of nested magnetic surfaces (note that, in general, the Clebsch representation does not presuppose the existence of a surface label).

Setting $\frac{\partial\rho}{\partial z}|_{in} = 0$ and noting that $B_r|_{in} = 0$ together with the property $\mathbf{B} \cdot \nabla\rho = 0$, we obtain

$$\nabla\rho|_{in} = \frac{\partial\rho}{\partial r}|_{in} \nabla r = \mathcal{L} \nabla r, \quad (2.2)$$

where we introduced the dimensionless quantity $\mathcal{L} = \frac{\partial\rho}{\partial r}|_{in}$, which will appear several times in the following. To complete the determination of the initial conditions, we set $\frac{\partial\nu}{\partial r}|_{in} = 0$, thus

$$\nabla\nu|_{in} = \frac{\partial\nu}{\partial z}|_{in} \nabla z + \frac{\partial\nu}{\partial\phi}|_{in} \nabla\phi. \quad (2.3)$$

Now, in order to obtain the representation (2.1), we postulate

$$\frac{\partial\nu}{\partial z}|_{in} = \frac{-B_\phi}{\mathcal{L}B_a}|_{in} = \frac{-B_{\phi,in}}{\mathcal{L}B_a} \quad (2.4)$$

and

$$\frac{\partial\nu}{\partial\phi}|_{in} = \frac{rB_z}{\mathcal{L}B_a}|_{in} = \frac{r_{in}B_{z,in}}{\mathcal{L}B_a}. \quad (2.5)$$

We remark that conditions (2.4) and (2.5) imply that $\mathbf{B} \cdot \nabla\nu = 0$.

2.1.2 Generic Coordinate System (GCS)

This coordinate system has the special property that the surface label is not defined on the basis of a flux quantity. In principle, through the FLT procedure, it is possible to construct a surface label without presupposing knowledge of the

fluxes. This approach can be advantageous when the flux information is numerically unreliable (e.g. regions close to the separatrix or islands, especially for stellarator configurations) or when the magnetic surfaces themselves cease to exist (e.g. stochastic regions). In fact, in the latter case, the GCS has no counterpart.

We postulate the system $(\tilde{\rho}, \tilde{\nu}, \chi)$ (thereafter, quantities corresponding to the GCS will be denoted by tilde). Compared to the FCS, the new Clebsch coordinates $\tilde{\rho}$ and $\tilde{\nu}$ retain dimensions of length, while the field following coordinate χ remains the same.

In a manner similar to the FCS case, the representation of the field line

$$\mathbf{B} = B_a \nabla \tilde{\rho} \times \nabla \tilde{\nu} \quad (2.6)$$

is generated by applying the initial conditions

$$\nabla \tilde{\rho} \Big|_{in} = \nabla r \quad (2.7)$$

and

$$\nabla \tilde{\nu} \Big|_{in} = \frac{-B_{\phi,in}}{B_a} \nabla z + \frac{r_{in} B_{z,in}}{B_a} \nabla \phi, \quad (2.8)$$

the main difference being that in the expressions (2.7) and (2.8), only the magnetic field is involved, i.e., we tacitly assume

$$\tilde{\mathcal{L}} \equiv \frac{\partial \tilde{\rho}}{\partial r} \Big|_{in} = 1. \quad (2.9)$$

This condition establishes a link between the GCS and the FCS. Indeed, considering the functional dependence $\tilde{\rho} = \tilde{\rho}(\rho)$, we get at the initial point

$$\frac{\partial \tilde{\rho}}{\partial r} \Big|_{in} = \frac{d\tilde{\rho}}{d\rho} \Big|_0 \frac{\partial \rho}{\partial r} \Big|_{in} \quad (2.10)$$

or

$$\tilde{\mathcal{L}} = \frac{d\tilde{\rho}}{d\rho} \Big|_0 \mathcal{L} \quad (2.11)$$

from which, with the aid of (2.9), we derive the relation between the surface labels

$$\frac{d\tilde{\rho}}{d\rho} \Big|_0 = \mathcal{L}^{-1}. \quad (2.12)$$

Furthermore, on the surface $\rho = \rho_0$ we have

$$\mathbf{B} = B_a \nabla \tilde{\rho} \times \nabla \tilde{\nu} = B_a \frac{d\tilde{\rho}}{d\rho} \Big|_0 \nabla \rho \times \nabla \tilde{\nu} = B_a \nabla \rho \times \nabla \nu, \quad (2.13)$$

so it holds

$$\tilde{\nu} = \mathcal{L} \nu. \quad (2.14)$$

2.2 Verification of the coordinate systems

Here, we present several diagnostics in order to evaluate the quality of the numerically generated systems.

We start with the verification of the field-alignment, since this property is crucial for the accuracy of the gyrokinetic calculations. We focus only on the FCS, since things are similar for the GCS. From the representation

$$\mathbf{B} = B_a \nabla \rho \times \nabla \nu \quad (2.15)$$

one readily gets

$$(B/B_a)^2 = g^{\rho\rho} g^{\nu\nu} - (g^{\rho\nu})^2. \quad (2.16)$$

We proceed with the calculation of the stream function $J\mathbf{B} \cdot \nabla \chi$, where J is the Jacobian of the transformation from the cylindrical to the magnetic system. Indeed, from the representation (2.15), we obtain

$$\mathbf{B} \cdot \nabla \chi = B_a \nabla \rho \times \nabla \nu \cdot \nabla \chi = B_a J^{-1} \quad (2.17)$$

therefore, along the field line, it should numerically hold

$$J\mathbf{B}^\chi = B_a. \quad (2.18)$$

The verification of expressions (2.16) and (2.18) is presented in Fig. 1.

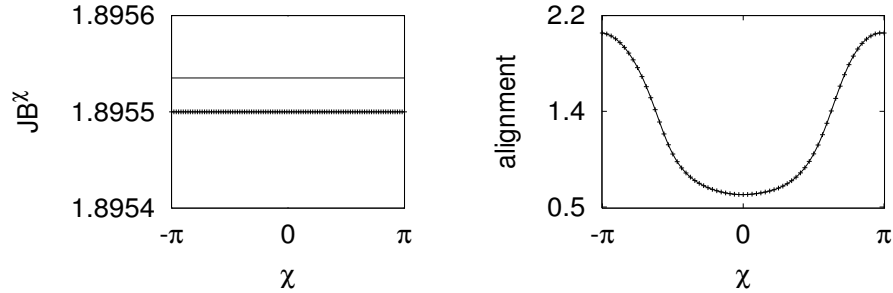


Figure 1: (Left) Numerical calculation of the stream function (line) to be compared with the value of B_a (crosses). (Right) Verification of the field-alignment property. The squared normalized magnetic field $(B/B_a)^2$ is shown with the line, while the metric combination $g^{\rho\rho} g^{\nu\nu} - (g^{\rho\nu})^2$ is depicted by the crosses.

Following, we derive the analytical relations connecting several geometric quantities appearing in the gyrokinetic setup between the two systems. For the

metric elements, in view of (2.12) and (2.14), it holds (for simplicity, we denote $g^{12} = \nabla\rho \cdot \nabla\nu$, $\tilde{g}^{12} = \nabla\tilde{\rho} \cdot \nabla\tilde{\nu}$ etc.)

$$\tilde{g}^{11} = \nabla\tilde{\rho} \cdot \nabla\tilde{\rho} = \left(\frac{d\tilde{\rho}}{d\rho} \Big|_0 \right)^2 \nabla\rho \cdot \nabla\rho = \mathcal{L}^{-2} g^{11}, \quad (2.19)$$

$$\tilde{g}^{12} = \nabla\tilde{\rho} \cdot \nabla\tilde{\nu} = \mathcal{L}^{-1} \nabla\rho \cdot \mathcal{L} \nabla\nu = g^{12}, \quad (2.20)$$

$$\tilde{g}^{22} = \nabla\tilde{\nu} \cdot \nabla\tilde{\nu} = \mathcal{L}^2 g^{22}. \quad (2.21)$$

Next, we relate the curvature components between the two systems,

$$\tilde{\omega}_1 = \mathbf{b} \times \nabla B \cdot \nabla\tilde{\rho} = \mathcal{L}^{-1} \mathbf{b} \times \nabla B \cdot \nabla\rho = \mathcal{L}^{-1} \omega_1 \quad (2.22)$$

and

$$\tilde{\omega}_2 = \mathbf{b} \times \nabla B \cdot \nabla\tilde{\nu} = \mathcal{L} \mathbf{b} \times \nabla B \cdot \nabla\nu = \mathcal{L} \omega_2. \quad (2.23)$$

For the numerical realization, we select the surface identified by $\rho = 0.60348m$ and compute the quantity $\mathcal{L} = 1.661$, by exploiting the information contained in the database (specifically, the ρ -profile of the major and minor radii at the elevation of the magnetic axis). Based on the description in Section 2.1, we are now able to generate both coordinate systems and extract the required geometric components.

Shown in Fig. 2 are the three metric elements and the Jacobian for both systems. The solid lines correspond to quantities for the FCS, whereas the dashed ones (wherever appearing) represent the GCS. To facilitate comparison, the crosses signify again quantities related to the GCS, although this time appropriately rescaled. For instance, in the left upper panel, they depict the rescaled metric $\mathcal{L}^2 \tilde{g}^{11}$, according to (2.19). Similarly, in the right upper panel, the crosses show the rescaled metric $\mathcal{L}^{-2} \tilde{g}^{22}$, according to (2.21). In the panels where the dashed lines are absent, it is implied that these quantities should be identical for both systems without rescaling. Note that the Jacobian is expected to be equal for the two systems, in view of the same stream functions. In Fig. 3 we present the numerical output for the curvature components. Again, the results related to the FCS are depicted by solid lines, whereas those for the GCS by dashed lines. The crosses indicate the rescaled quantities for the GCS following (2.22) and (2.23).

For the purpose of gyrokinetic simulations in the framework of a flux tube approach, the value of the global shear \hat{s} is often required. For the FCS, applying the usual parallel boundary condition to a typical scalar field A [16]

$$A(\rho, \nu(\theta + 2\pi, \phi), \theta + 2\pi) = A(\rho, \nu(\theta, \phi), \theta) \quad (2.24)$$

and performing a standard Fourier analysis, we obtain the (dimensionless) expression

$$\hat{s} = \frac{1}{2\pi B_a} \frac{d\Psi_p}{d\rho} \Big|_0 \frac{dq}{d\rho} \Big|_0, \quad (2.25)$$

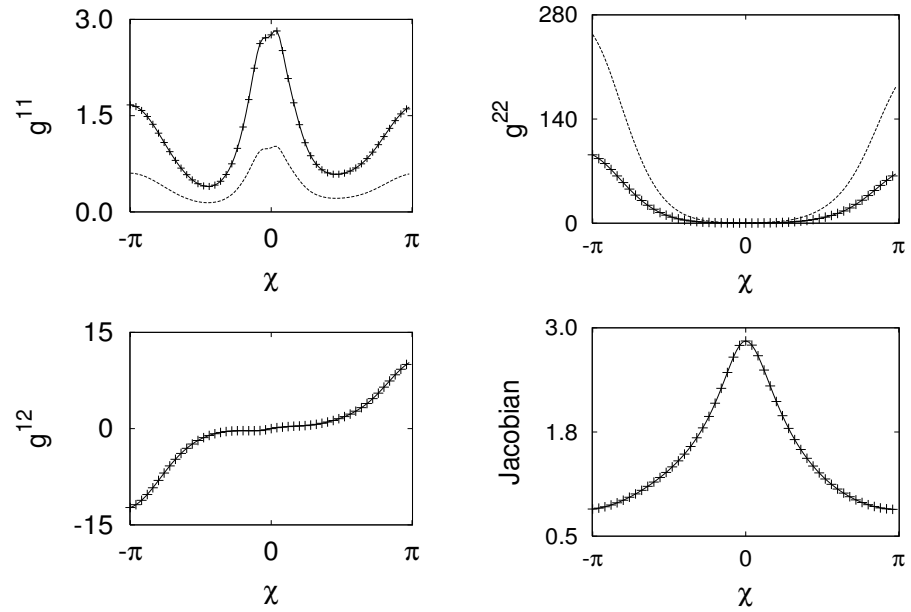


Figure 2: Metric elements and Jacobian for the two coordinate systems. The solid lines correspond to the FCS, the dashed lines and the crosses to the GCS (see text for explanation).

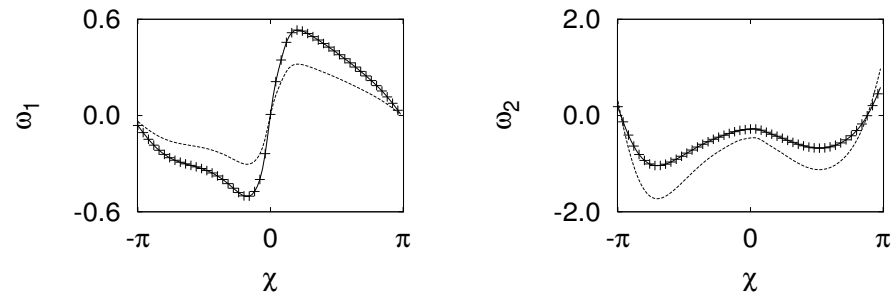


Figure 3: Curvature components for the two coordinate systems. The solid lines correspond to the FCS, the dashed lines and the crosses to the GCS (see text for explanation).

or, using the definition of the flux label ρ , we end up with the familiar form

$$\hat{s} = \frac{\rho_0}{q_0} \frac{dq}{d\rho} \Big|_0. \quad (2.26)$$

Now, the shear for the GCS is related to \hat{s} through

$$\tilde{\hat{s}} = \frac{1}{2\pi B_a} \frac{d\Psi_p}{d\tilde{\rho}} \Big|_0 \frac{dq}{d\tilde{\rho}} \Big|_0 = \mathcal{L}^2 \hat{s}. \quad (2.27)$$

Another important quantity, especially in the context of stellarator configurations but also for tokamak studies in the edge region, is the local shear S_{loc} , whose surface average by definition equals the global shear \hat{s} . In Appendix I, it is shown that for the FCS it holds

$$S_{loc} = -J \mathbf{h} \cdot \nabla \times \mathbf{h} \quad \text{with} \quad \mathbf{h} = \frac{\mathbf{B} \times \nabla \rho}{g^{11} B_a}. \quad (2.28)$$

Note that the same transformation rule as in (2.27) applies to the local shear for the GCS, i.e.

$$\tilde{S}_{loc} = \mathcal{L}^2 S_{loc}. \quad (2.29)$$

At this point, we provide an additional verification test. We generate a set of flux tubes, each on a different flux surface and for these we calculate S_{loc} . Then, we compute the flux averages using the rule

$$\langle S_{loc} \rangle = \frac{\int_{-\pi}^{\pi} J S_{loc} d\chi}{\int_{-\pi}^{\pi} J d\chi}. \quad (2.30)$$

These values of $\langle S_{loc} \rangle$ should be equal, within numerical errors, to the values of the global shear which can be readily extracted from the database. In Fig. 4, we display the result of this non-trivial test. It is clearly seen that the values determined by the two methods are in very good agreement.

2.3 Comparison and interpretation of ITG simulation results

We are now ready to present and discuss simulation results for a linear ITG instability, after implementing each coordinate system into the gyrokinetic code GENE. Our goal is to demonstrate that the physics output is insensitive to the coordinate system employed. As will be clear in the following, this procedure calls for a proper handling of the parameters controlling the instability.

The driving mechanism of the ITG instability is attributed to the advection term appearing in the Vlasov gyrokinetic equation, which involves the radial ion temperature gradient (in principle, the density gradient may also contribute) [14]

$$\frac{\mathbf{b} \times \nabla \Phi}{B} \cdot \frac{\nabla T_i}{T_i} F_{i0}, \quad (2.31)$$

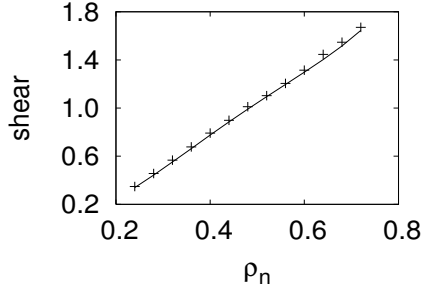


Figure 4: Global shear as a function of the normalized radius for the DIII-D configuration, calculated by the database (line) and TRACER (crosses).

where Φ denotes the gyro-averaged potential, F_{i0} is the equilibrium (Maxwellian) distribution for the ions and T_i is the background ion temperature. Once expanded on the FCS and Fourier transformed (for the purposes of numerical treatment), expression (2.31) becomes

$$i k_y L_{T_i}^{-1} \frac{\Phi}{B_a} F_{i0} \quad (2.32)$$

where $L_{T_i}^{-1} = \frac{1}{T_i} \frac{dT_i}{d\rho}$. In the context of the GCS, the analogous term reads

$$i \tilde{k}_y \tilde{L}_{T_i}^{-1} \frac{\Phi}{B_a} F_{i0} \quad (2.33)$$

with $\tilde{L}_{T_i}^{-1} = \frac{1}{T_i} \frac{dT_i}{d\rho}$.

In order to connect the two pictures, the key link is the invariance of the Vlasov equation under coordinate transformations. Therefore, between the two coordinate systems, the following constraint must hold

$$k_y L_{T_i}^{-1} = \tilde{k}_y \tilde{L}_{T_i}^{-1}. \quad (2.34)$$

Now, since the temperature gradients for the two coordinate systems are related through

$$\tilde{L}_{T_i}^{-1} = \mathcal{L} L_{T_i}^{-1}, \quad (2.35)$$

the mapping between the k_y spectra will read

$$\tilde{k}_y = \mathcal{L}^{-1} k_y. \quad (2.36)$$

Expressions (2.35) and (2.36) are fundamental for the interpretation of the gyrokinetic results. In order to proceed with a direct comparison of the physics output,

one has to make certain that these constraints are simultaneously satisfied for the two coordinate systems through the input parameters.

In the light of these findings, we perform linear ITG calculations corresponding to the two coordinate systems. [The electron dynamics is assumed to be adiabatic, the density profile flat and the electron to ion temperature ratio equal to unity.] In particular, we carry out a scan of growth rates and frequencies over the binormal wavenumber spectrum k_y (normalized with respect to $\rho_s = c_s/\Omega_i$, where c_s is the ion sound speed and Ω_i is the ion Larmor frequency). Setting the (normalized) temperature gradient equal to $\alpha L_{T_i}^{-1} = 2.356$ for the FCS (here, $\alpha = 0.592m$ is half the diameter of the last closed flux surface (LCFS)), the constraint (2.35) adjusts the gradient for the GCS to $\alpha \tilde{L}_{T_i}^{-1} = 2.356 \mathcal{L} = 3.913$. In addition, given a set of binormal wavenumbers for the FCS, we select proper values for the GCS, so that the rule (2.36) is fulfilled.

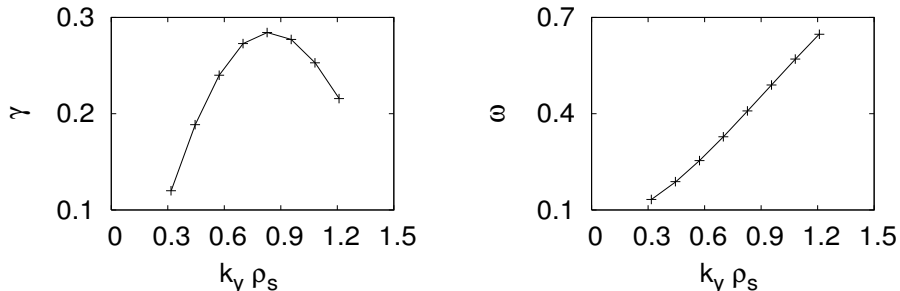


Figure 5: Growth rates in units of $\frac{c_s}{\alpha}$ (left) and frequencies in units of $\frac{c_s}{\alpha}$ (right) from the linear ITG calculations based on the FCS (line) and the GCS (crosses).

In Fig. 5, the growth rates and frequencies based on the FCS and the GCS are presented. The values are identical proving the consistency of the calculations.

3 Benchmark of gyrokinetic codes for a numerical tokamak equilibrium

In this section, we carry out a similar analysis as before, this time involving the gyrokinetic codes GS2 and GENE. As will be discussed presently, the employed coordinate systems and, as a consequence of this, the geometric components are not identical.

For this application, the coordinate system for GENE is the FCS, analyzed in detail in Section 2.1.1. Therefore, we only present here the coordinate setup for GS2. Let us postulate the following dimensionless quantities, thereafter denoted

by the subscript “N”:

$$\rho_N = \frac{\rho}{\rho_0}, \quad \Psi_N = \frac{\Psi_p}{2\pi\alpha^2 B_a}, \quad B_N = \frac{B}{B_a}, \quad \nabla_N = \alpha \nabla \quad (3.1)$$

where Ψ_p denotes the poloidal flux, $\rho_0 = 0.754m$ is the averaged minor radius at the LCFS and $\alpha = 0.592m$ as before. Now, the coordinate system for GS2 reads (ρ_N, ν_N, θ) , where $\nu_N = \Psi'_{N0}(q\theta - \phi)$. Here, the prime denotes differentiation with respect to ρ_N . We notice that the field following coordinate is the poloidal angle θ (in contrast to the FCS, where the coordinate χ is closely related to the toroidal angle). Finally, the field representation for GS2 becomes

$$\mathbf{B}_N = \nabla_N \rho_N \times \nabla_N (\Psi'_{N0}(q\theta - \phi)). \quad (3.2)$$

3.1 Relations for geometric elements and simulation parameters

We derive the equations relating the geometric elements as well as the temperature gradients and k_y spectra for the two codes. For the metric coefficients, we successively obtain

$$\begin{aligned} g_{\text{GS2}}^{11} &= \nabla_N \rho_N \cdot \nabla_N \rho_N \\ &= (\alpha \nabla) \left(\frac{\rho}{\rho_0} \right) \cdot (\alpha \nabla) \left(\frac{\rho}{\rho_0} \right) \\ &= \left(\frac{\alpha}{\rho_0} \right)^2 g_{\text{GENE}}^{11}, \end{aligned} \quad (3.3)$$

$$\begin{aligned} g_{\text{GS2}}^{12} &= \nabla_N \rho_N \cdot \nabla_N (\Psi'_{N0}(q\theta - \phi)) \\ &= (\alpha \nabla) \left(\frac{\rho}{\rho_0} \right) \cdot (\alpha \nabla) \left(\frac{\rho_0}{\alpha^2} \frac{\dot{\Psi}_{p0}}{2\pi B_a} (q\theta - \phi) \right) \\ &= g_{\text{GENE}}^{12}, \end{aligned} \quad (3.4)$$

and similarly

$$g_{\text{GS2}}^{22} = \left(\frac{\rho_0}{\alpha} \right)^2 g_{\text{GENE}}^{22}. \quad (3.5)$$

We continue with the curvature terms. In the GS2 formulation, the relevant quantities are

$$\begin{aligned} \omega_1^{\text{GS2}} &= \frac{2}{B_N^2} \Psi'_{N0} q'_0 \mathbf{b} \times \nabla_N B_N \cdot \nabla_N \rho_N \\ &= \frac{2}{B_N^2} \Psi'_{N0} q'_0 \frac{\alpha^2}{B_a \rho_0} \mathbf{b} \times \nabla B \cdot \nabla \rho \end{aligned} \quad (3.6)$$

and

$$\begin{aligned}\omega_2^{\text{GS2}} &= \frac{2}{B_N^2} \mathbf{b} \times \nabla_N B_N \cdot \nabla_N \nu_N \\ &= \frac{2}{B_N^2} \frac{\rho_0}{B_a} \mathbf{b} \times \nabla B \cdot \nabla \nu_N.\end{aligned}\quad (3.7)$$

In order to connect with the GENE formulation, we expand the triple products on the FCS (see Appendix II for details). For instance,

$$\mathbf{b} \times \nabla B \cdot \nabla \rho = -B_N \frac{\partial B}{\partial \nu} - B_N \frac{g_{\text{GENE}}^{11} g_{\text{GENE}}^{23} - g_{\text{GENE}}^{12} g_{\text{GENE}}^{13}}{g_{\text{GENE}}^{11} g_{\text{GENE}}^{22} - (g_{\text{GENE}}^{12})^2} \frac{\partial B}{\partial \chi}, \quad (3.8)$$

therefore (3.6) becomes

$$\begin{aligned}\omega_1^{\text{GS2}} &= -2 \frac{\alpha}{\rho_0} \Psi'_{N0} q'_0 \frac{\alpha}{B} \left(\frac{\partial B}{\partial \nu} + \frac{g_{\text{GENE}}^{11} g_{\text{GENE}}^{23} - g_{\text{GENE}}^{12} g_{\text{GENE}}^{13}}{g_{\text{GENE}}^{11} g_{\text{GENE}}^{22} - (g_{\text{GENE}}^{12})^2} \frac{\partial B}{\partial \chi} \right) \\ &= \frac{\alpha}{\rho_0} \Psi'_{N0} q'_0 \omega_1^{\text{GENE}}.\end{aligned}\quad (3.9)$$

In the same fashion, we obtain

$$\begin{aligned}\omega_2^{\text{GS2}} &= 2 \frac{\rho_0}{\alpha} \frac{\alpha}{B} \left(\frac{\partial B}{\partial \rho} - \frac{g_{\text{GENE}}^{12} g_{\text{GENE}}^{23} - g_{\text{GENE}}^{22} g_{\text{GENE}}^{13}}{g_{\text{GENE}}^{11} g_{\text{GENE}}^{22} - (g_{\text{GENE}}^{12})^2} \frac{\partial B}{\partial \chi} \right) \\ &= \frac{\rho_0}{\alpha} \omega_2^{\text{GENE}}.\end{aligned}\quad (3.10)$$

Furthermore, we derive the relations for the key parameters in the context of the flux tube gyrokinetic simulations, namely the normalized ion temperature gradient (*nitg*) and the probed wavenumber k_y . For the former, it holds

$$(\textit{nitg})_{\text{GENE}} = \frac{\alpha}{T} \frac{dT}{d\rho} = \frac{\alpha}{\rho_0} \frac{1}{T} \frac{dT}{d\rho_N} = \frac{\alpha}{\rho_0} (\textit{nitg})_{\text{GS2}}. \quad (3.11)$$

Now, the invariance of the Vlasov equation with respect to coordinate transformations imposes the rule (see also (2.34))

$$(\textit{nitg})_{\text{GENE}} k_y^{\text{GENE}} = (\textit{nitg})_{\text{GS2}} k_y^{\text{GS2}}, \quad (3.12)$$

which in turn implies that, for the comparison of the physics output, e.g. in the context of a k_y scan, one has to take into account the rule

$$k_y^{\text{GENE}} = \frac{\rho_0}{\alpha} k_y^{\text{GS2}}. \quad (3.13)$$

3.2 Comparison of geometric quantities and gyrokinetic results

In order to set the stage for the benchmarks, we employ the DIII-D configuration described before, and generate the same flux tube for both codes, characterized by $\rho_N = 0.8$ and $\nu_N = 0$. First, we perform direct numerical comparisons of the geometric quantities on the basis of the relations derived above. [A word of caution is in place here: since the two codes use a different definition for the parallel coordinate, we map the GENE output onto the poloidal angle θ to facilitate comparison. However, for the gyrokinetic simulations, the coordinate χ is always used.] All geometry related data presented here comes from the TRACER code for the GENE setup, while for GS2 a separate geometry module is recruited based on ideal MHD calculations [17]. As an additional piece of information, in Fig. 6, it is demonstrated that the normalized magnetic field itself as well as the normalized component $\mathbf{b} \cdot \nabla_N \theta = \alpha b^\theta$ coincide. This result guarantees that we indeed consider the same flux tube for both codes.

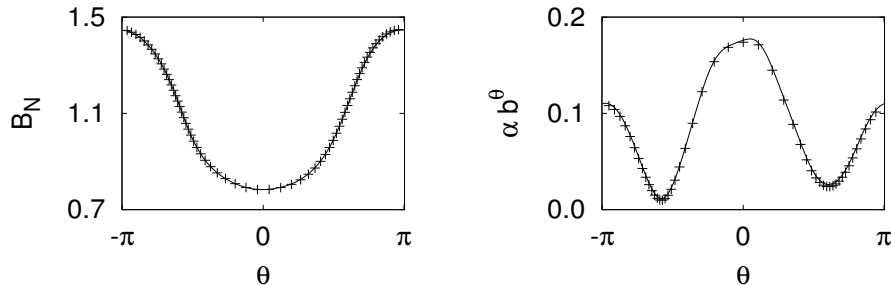


Figure 6: (Left) Comparison of the normalized magnetic field for GS2 (line) and GENE (crosses). (Right) Same for the normalized component.

We proceed with the comparison of the metric elements. The rules relating these quantities for the two codes are given by expressions (3.3)-(3.5). The numerical output appears in Fig. 7, showing very good agreement, once the quantities for GENE have been rescaled, where appropriate. Moreover, the metric combination $g^{11}g^{22} - (g^{12})^2$, appearing in the same figure, is practically equal for both codes and, at the same time, equal to the squared normalized magnetic field (see Section 2.2). The last part of the geometry comparison comprises the two curvature components, which demonstrate excellent agreement (see Fig. 8), again after rescaling the quantities referring to GENE, according to (3.3) and (3.5).

In the remainder of this section, we will present and discuss results from a linear ITG instability, produced by GENE and GS2. In order to evaluate the quality of the benchmarks, we use the simple \hat{s} - α model as norm, for which no special transformations are required. The relevant comparison appears in

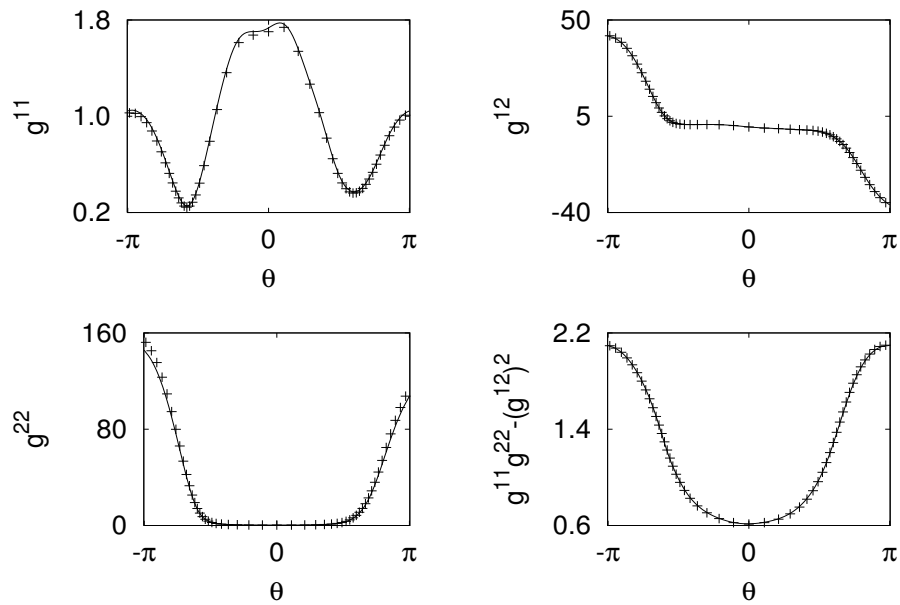


Figure 7: Comparison of the metric elements for GS2 (line) and GENE (crosses) after rescaling.

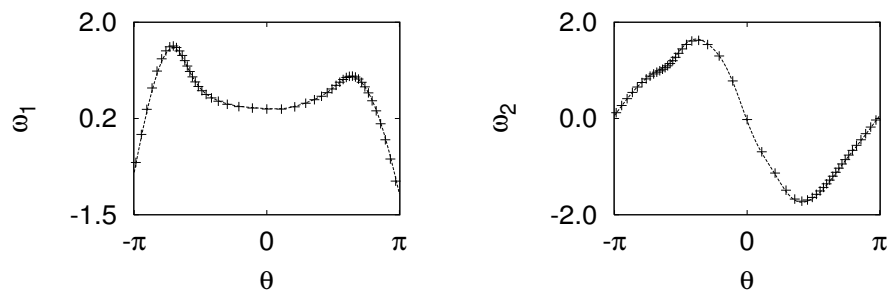


Figure 8: Comparison of the curvature components for GS2 (line) and GENE (crosses) after rescaling.

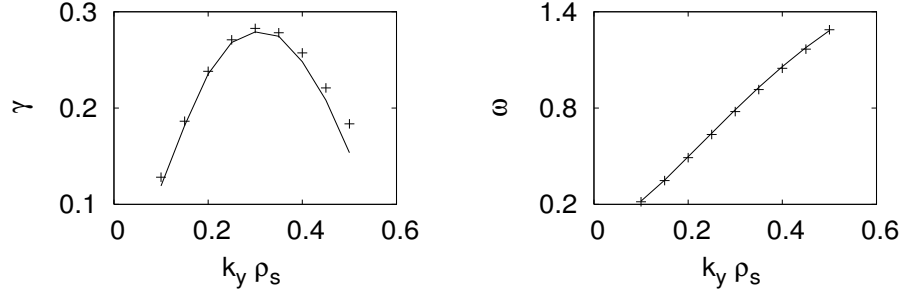


Figure 9: k_y scan for \hat{s} - α geometry from GS2 (line) and GENE (crosses). (Left) Comparison of the growth rates in units of c_s/R . (Right) Comparison of the frequencies in units of c_s/R , where R is the major radius.

Fig. 9. For the DIII-D case, the linear properties of the instability as a function of the probed wavenumber k_y are displayed in Fig. 10. Specifically, we have selected $(nitg)_{\text{GS2}} = 3$, therefore for GENE we prescribe $(nitg)_{\text{GS2}} = 2.35$ according to the rule (3.11). For these calculations, it is assumed that the normalized ion density gradient ($nidg$) also contributes to the instability, i.e., we set $(nidg)_{\text{GS2}} = 1$ and, accordingly, $(nidg)_{\text{GENE}} = 0.78$. At the same time, we should take into account the rule connecting the binormal wavenumbers, suggested by (3.13). For the purposes of the $k_y \rho_s$ scan, we have chosen for GS2 the series $k_y^{\text{GS2}} \rho_s = [0.25, 0.30, 0.35, \dots, 1.0]$, thus for GENE, one should postulate $k_y^{\text{GENE}} \rho_s = [0.32, 0.45, 0.57, \dots, 1.27]$, respectively. Only then are the growth rates and frequencies readily comparable. The results demonstrate that the gyrokinetic computations from the two codes using an MHD equilibrium agree with each other to the same degree as with the \hat{s} - α configuration.

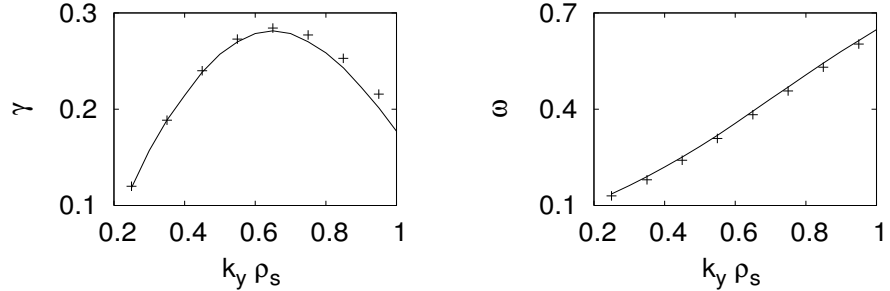


Figure 10: k_y scan for DIII-D equilibrium from GS2 (line) and GENE (crosses). (Left) Comparison of the growth rates in units of c_s/α . (Right) Comparison of the frequencies in units of c_s/α .

4 Conclusions

The aim of this work is to draw attention to the diversity of field-aligned coordinate systems generated numerically from magnetohydrodynamic equilibria, in the context of linear gyrokinetic simulations. As was clearly demonstrated through a pragmatic approach, certain steps should be taken before systematic benchmarks between gyrokinetic codes with different geometry implementation are carried out.

More specifically, it is important to ascertain that the geometric elements, which are usually prepared through different modules for the various gyrokinetic solvers, are in good agreement. That this is the case for the codes GENE and GS2 was shown here by performing extensive numerical comparisons. At the same time, certain diagnostics were exploited in order to verify the quality of the magnetic coordinate systems. As a second step, a necessary transformation procedure, involving the temperature/density gradients and the binormal spectra k_y , was described in order to compare the physics results. Having done this, we performed ITG gyrokinetic simulations with these codes, and obtained quantitative agreement when working with an EFIT equilibrium for the tokamak DIII-D, of the same level as with the model $\hat{s} - \alpha$ configuration.

The present analysis was restricted to the axisymmetric case and, of course, it is of major concern to generalize it for three dimensional equilibria, in the context of simulations in stellarator geometry. However, this effort is more complicated, since it calls for several additional modules, such as the extended equilibrium code VMEC [18], as well as the codes TERPSICHORE [19] and VVBAL [20], which prepare the geometric elements for GS2 (for GENE, the TRACER code is again utilized), and therefore it is deferred to a separate upcoming publication.

Appendix I: Local shear for the FCS

We provide the expression for the local shear S_{loc} associated with the FCS and we formally prove its consistency on the grounds that the flux average of the local shear should be equal to the global shear \hat{s} .

Our basis is the field representation

$$\mathbf{B} = B_a \nabla \rho \times \nabla \nu, \quad \text{with} \quad \nu = \frac{\dot{\Psi}_{p0}}{2\pi B_a} (q\theta - \phi). \quad (\text{AI-1})$$

Now, we claim that the proper definition for the local shear is

$$S_{loc} = -J \mathbf{h} \cdot \nabla \times \mathbf{h}, \quad \text{with} \quad \mathbf{h} = \frac{\mathbf{B} \times \nabla \rho}{g^{\rho\rho} B_a}. \quad (\text{AI-2})$$

The Jacobian of the system is determined as follows

$$J^{-1} = \nabla \rho \times \nabla \nu \cdot \nabla \chi = \frac{\dot{\Psi}_{p0}}{2\pi B_a} (\nabla \rho \times \nabla \theta \cdot \nabla \phi). \quad (\text{AI-3})$$

Using the representation (AI-1) in the definition of \mathbf{h} , after some straightforward algebra, we obtain

$$\begin{aligned} \mathbf{h} &= \frac{\dot{\Psi}_{p0}}{2\pi B_a} \left(\frac{g^{\rho\phi} - q g^{\rho\theta}}{g^{\rho\rho}} \nabla \rho + q \nabla \theta - \nabla \phi \right), \\ \nabla \times \mathbf{h} &= \frac{\dot{\Psi}_{p0}}{2\pi B_a} \left(\nabla \left(\frac{g^{\rho\phi} - q g^{\rho\theta}}{g^{\rho\rho}} \right) \times \nabla \rho + \dot{q} \nabla \rho \times \nabla \theta \right) \end{aligned} \quad (\text{AI-4})$$

and finally

$$S_{loc} = \frac{\dot{\Psi}_{p0}}{2\pi B_a} \left(\dot{q} - (\partial_\theta + q \partial_\phi) \left(g^{\rho\phi} - \frac{q g^{\rho\theta}}{g^{\rho\rho}} \right) \right). \quad (\text{AI-5})$$

Taking the flux average, we end up with

$$\langle S_{loc} \rangle = \frac{\dot{\Psi}_{p0}}{2\pi B_a} \dot{q}_0, \quad (\text{AI-6})$$

thus retrieving the expression of \hat{s} for the FCS (see also (2.25)).

Based on the representation (AI-1), we rewrite (AI-5) in a form which lends itself to numerical evaluation via the FLT method. Successively, we have

$$\begin{aligned} \mathbf{h} &= \nabla \nu - \frac{g^{\rho\nu}}{g^{\rho\rho}} \nabla \rho, \\ \nabla \times \mathbf{h} &= \nabla \rho \times \nabla \left(\frac{g^{\rho\nu}}{g^{\rho\rho}} \right), \\ \mathbf{h} \cdot \nabla \times \mathbf{h} &= -\frac{1}{B_a} \mathbf{B} \cdot \nabla \left(\frac{g^{\rho\nu}}{g^{\rho\rho}} \right). \end{aligned}$$

Further we notice that, along the field line, it holds $\mathbf{B} \cdot \nabla = B^\chi \frac{d}{d\chi}$, thus

$$S_{loc} = \frac{JB^\chi}{B_a} \frac{d}{d\chi} \left(\frac{g^{\rho\nu}}{g^{\rho\rho}} \right). \quad (\text{AI-7})$$

As a final step, we substitute the value of the stream function (see (2.18)), thus

$$S_{loc} = \frac{d}{d\chi} \left(\frac{g^{\rho\nu}}{g^{\rho\rho}} \right). \quad (\text{AI-8})$$

The form (AI-8) is most suitable for calculating the local shear with the TRACER code.

Appendix II: Proof of expression (3.8)

In the following, we attempt to generalize, rather than prove expression (3.8). Specifically, consider a Clebsch coordinate system (v^1, v^2, v^3) , then for any scalar functions A, G , it holds

$$\begin{aligned} (\mathbf{b} \times \nabla A) \cdot \nabla G &= Jb^3 \left((g^{11}g^{22} - (g^{12})^2) [\partial_1 A, \partial_2 G] \right. \\ &\quad + (g^{11}g^{23} - g^{12}g^{13}) [\partial_1 A, \partial_3 G] \\ &\quad \left. + (g^{12}g^{23} - g^{22}g^{13}) [\partial_2 A, \partial_3 G] \right), \end{aligned} \quad (\text{AII-1})$$

where we introduced the commutator

$$[\partial_i A, \partial_j G] = \partial_i A \partial_j G - \partial_i G \partial_j A, \quad i, j = 1, \dots, 3. \quad (\text{AII-2})$$

We proceed with the proof of expression (AII-1) as follows (repeated indices are summed)

$$\begin{aligned} \mathbf{b} \times \nabla A &= b^3 \partial_i A e_3 \times e^i = Jb^3 \partial_i A (e^1 \times e^2) \times e^i \\ &= Jb^3 \left((g^{11}e^2 - g^{12}e^1) \partial_1 A + (g^{12}e^2 - g^{22}e^1) \partial_2 A \right. \\ &\quad \left. + (g^{13}e^2 - g^{23}e^1) \partial_3 A \right). \end{aligned} \quad (\text{AII-3})$$

Then,

$$(\mathbf{b} \times \nabla A) \cdot \nabla G = (\mathbf{b} \times \nabla A) \cdot e^j \partial_j G \quad (\text{AII-4})$$

which, on substitution of the expression (AII-3), readily gives (AII-1).

In order to prove expression (3.8), we postulate $A = B$, $G = \rho$, $v^1 = \rho$, $v^2 = \nu$ and $v^3 = \chi$, thus

$$\begin{aligned} (\mathbf{b} \times \nabla B) \cdot \nabla \rho &= -Jb^3 \left((g^{11}g^{22} - (g^{12})^2) \frac{\partial B}{\partial \nu} + (g^{11}g^{23} - g^{12}g^{13}) \frac{\partial B}{\partial \chi} \right) \\ &= -Jb^3 (g^{11}g^{22} - (g^{12})^2) \left(\frac{\partial B}{\partial \nu} + \frac{g^{11}g^{23} - g^{12}g^{13}}{g^{11}g^{22} - (g^{12})^2} \frac{\partial B}{\partial \chi} \right). \end{aligned} \quad (\text{AII-5})$$

Now, we notice that, given the representation $\mathbf{B} = B_a \nabla v^1 \times \nabla v^2$, we get

$$Jb^3 (g^{11}g^{22} - (g^{12})^2) = Jb^3 \frac{B^2}{B_a^2} = JB^3 \frac{B}{B_a^2} = B_a \frac{B}{B_a^2} = \frac{B}{B_a} = B_N. \quad (\text{AII-6})$$

This concludes the proof for the expression (3.8).

References

- [1] W. D. D’Haeseleer, W. N. G. Hitchon, J. D. Callen, J. L. Shohet, Flux Coordinates and Magnetic Field Structure (Springer, Berlin, 1991).
- [2] A. M. Dimits et al., Phys. Plasmas **7**, 969 (2000).
- [3] W. M. Nevins, S. E. Parker, Y. Chen, J. Candy, A. M. Dimits, W. Dorland, G. W. Hammett, and F. Jenko, Phys. Plasmas **7**, 969 (2000).
- [4] J. Candy and R. E. Waltz, W. Dorland, Phys. Plasmas **11**, L25 (2004).
- [5] C. Estrada-Mila, J. Candy and R. E. Waltz, Phys. Plasmas **12**, 022305 (2005).
- [6] R. L. Miller, M. S. Chu, J. M. Greene, Y. R. Lin-Liu and R. E. Waltz, Phys. Plasmas **5**, 973 (1998).
- [7] M. Kammerer, F. Merz and F. Jenko, Physics of Plasmas **15**, 052102 (2008)
- [8] G. Rewoldt, L. -P. Ku and W. M. Tang, Phys. Plasmas **12**, 102512 (2005).
- [9] V. Kornilov, R. Kleiber and R. Hatzky, Nucl. Fusion **45**, 238 (2005).
- [10] P. Xanthopoulos and F. Jenko, Phys. Plasmas **14**, 042501 (2007).
- [11] F. Jenko, W. Dorland, M. Kotschenreuther, and B. N. Rogers, Phys. Plasmas **7**, 1904 (2000).
- [12] W. Dorland, Ph.D thesis, Princeton University, 1993.
- [13] V. V. Nemov, Nucl. Fusion **28**, 1727 (1988).
- [14] P. Xanthopoulos and F. Jenko, Phys. Plasmas **13**, 092301 (2006).
- [15] T. Rhodes, priv. comm.
- [16] M. A. Beer, S. C. Cowley, and G. W. Hammett, Phys. Plasmas **2**, 2687 (1995).
- [17] C. M. Bishop, P. Kirby, J. W. Connor, R. J. Hastie and J. B. Taylor, Nucl. Fusion **24**, 1579 (1984).
- [18] S. P. Hirsmann and D. K. Lee, Comput. Phys. Commun. **39**, 161 (1981).
- [19] D. V. Anderson, W. A. Cooper, R. Gruber, S. Merazzi and U. Schwenn, Int. J. Supercomput. Appl. **4**, 34 (1990).
- [20] W. A. Cooper, Plasma Phys. Controlled Fusion **34**, 1011 (1992).